Protein ligand migration mapped by nonequilibrium 2D-IR exchange spectroscopy

Jens Bredenbeck*†, Jan Helbing*, Karin Nienhaus‡, G. Ulrich Nienhaus‡§, and Peter Hamm*

*Physikalisch-Chemisches Institut, Universität Zürich, Winterthurerstrasse 190, CH-8057 Zürich, Switzerland; ‡Institute of Biophysics, University of Ulm, Albert Einstein-Allee 11, 89081 Ulm, Germany; and §Department of Physics, University of Illinois at Urbana–Champaign, 1110 West Green Street, Urbana, IL 61801

Edited by Robin M. Hochstrasser, University of Pennsylvania, Philadelphia, PA, and approved November 16, 2006 (received for review September 6, 2006)

2D-IR exchange spectroscopy has been introduced recently to map chemical exchange networks in equilibrium with subpicosecond time resolution. Here, we demonstrate the generalization of 2D-IR exchange spectroscopy to nonequilibrium systems and its application to map light-triggered migration of ligands between different sites in a protein. Within picoseconds after a photodissociating laser pulse, carbon monoxide ligands relocate from their binding site A at the heme prosthetic group of myoglobin to a primary docking site B in the distal heme pocket. Multiple CO stretching bands are observed for the CO ligand in sites A and B, indicating that several distinct conformational substates of the myoglobin: ligand complex coexist in solution. Exchange cross-peaks between the bands associated with substates of heme-bound CO and photodissociated CO in the primary docking site reveal the substate connectivity at physiological temperature.

ligand binding | myoglobin | chemical exchange | infrared spectroscopy

Chemical and biochemical processes frequently involve networks of interconverting species and intermediates. 2D exchange spectroscopy (EXSY) was introduced in the field of NMR almost three decades ago as a powerful tool to map such networks (1). The connectivity between chemical species is revealed in 2D-NMR-EXSY spectra by off-diagonal peaks that are connected to the diagonal peaks of two interconverting species by horizontal and vertical lines. However, the two diagonal peaks coalesce because of motional line narrowing when the exchange rate is in the range of the frequency separation between the spectral lines of the interconverting species (2), so that faster processes cannot be observed. As a consequence, the time resolution of 2D-NMR-EXSY is fundamentally limited to the millisecond-to-second range.

By contrast, frequency separations of vibrational lines in IR spectra are in the THz range, and coalescence of vibrational lines occurs only for much more rapid exchange processes, i.e., on subpicosecond time scales. Thus, pulsed 2D-IR-EXSY experiments using femtosecond lasers make a new range of fast exchange phenomena accessible to real-time studies, as has been demonstrated recently with various 2D-IR approaches (3–5).

A regular 2D-IR-EXSY experiment relies on the interconversion of species to happen spontaneously during the waiting time between subsequent IR pulses (3). Here, we present an extension of 2D-IR-EXSY to the application on transient species (T2D-IR-EXSY), where exchange is triggered during the waiting time by an external perturbation, an additional laser pulse (6). Hence, EXSY on nonequilibrium systems that evolve on picosecond time scales becomes possible and pathways between intermediate states can be mapped.

An exciting application where T2D-IR-EXSY can fully unfold its potential is the light-induced migration of ligands between different sites in a protein, as is the case for myoglobin (Mb). Mb is probably the best-studied protein in the field of biophysics and earned itself the title "hydrogen atom of biology" (7). Still, several fundamental issues have remained unsettled. One of them is the connectivity between various states of the protein when the ligand is covalently bound at the heme or unbound within the heme pocket, especially under physiological conditions. This problem provides an excellent example for the possibilities opened up by the T2D-IR-EXSY approach.

Mb is a small heme protein that is believed to be responsible for oxygen storage and transport in muscle tissue. It can bind small ligands such as oxygen (O_2), nitric oxide (NO), or carbon monoxide (CO) at its heme iron. Associated with its biological function, the Mb:ligand complex features several conformational substates that coexist in solution (see refs. 7–10 and references therein). In MbCO, these different conformations are associated with distinct bands in the ligand's vibrational absorption spectrum, because of its exquisite sensitivity to the electric field generated by the local protein environment. In the CO-bound state of sperm whale Mb (sw-MbCO), three CO vibrational bands are observed that have been assigned to three conformational substates termed A_0, A_1, and A_3. Based on crystallographic studies, vibrational spectroscopy, and theoretical modeling, the differences in the IR absorption of the ligand among the A substates is attributed mainly to different conformations of His^{64}, which results in different electric fields at the binding site that produce different vibrational Stark shifts of the IR stretching mode of the heme-bound CO (see refs. 9 and 10 and references therein). The A_0 population is associated with a protonated His^{64} imidazole, which has a pK of 4.5, and is therefore small at neutral pH (11, 12). Substates A_1 and A_3 both have a neutral imidazole. Fluctuations between the A_1 and A_3 substates are much faster than exchange to A_0 (8), indicating smaller conformational changes. The lower frequency of A_3 as compared with A_1 reflects a closer proximity of the imidazole to the CO in A_3 (9, 10). Each A substate shows markedly different kinetics of CO rebinding after flash photolysis, implying different functional properties (8).

Upon photodissociation from the heme, CO migrates to a primary docking site (site B), which plays an important role in mediating ligand transport to and from the active site at the heme (10, 13). Docked in B, the CO again gives rise to several bands, B substates B_2, B_1, and B_0, which reflect a different structure of the protein and different orientation of the CO (10, 14, 15). Based on IR spectroscopic studies comparing different mutants and quantum chemical calculations, the picture has emerged that B_2 and B_1 correspond to CO residing in the primary docking site of Mb in the A_1 conformation, featuring opposite orientations with either the C or O atom pointing toward the Fe of the heme (10, 15–17).

Author contributions: J.B., J.H., G.U.N., and P.H. designed research; J.B., J.H., and K.N. performed research; K.N. and G.U.N. contributed new reagents/analytic tools; J.B., J.H., and P.H. analyzed data; and J.B., G.U.N., and P.H. wrote the paper.

The authors declare no conflict of interest.

This article is a PNAS Direct Submission.

Abbreviations: EXSY, exchange spectroscopy; Mb, myoglobin; sw-Mb, sperm whale Mb; h-Mb, horse heart Mb; TDS, temperature derivative spectroscopy.

†To whom correspondence should be addressed. E-mail: j.bredenbeck@pci.unizh.ch.

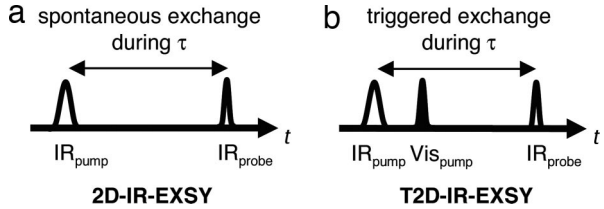

Fig. 1. 2D-IR pulse sequences. (*a*) Equilibrium 2D-IR-EXSY. Chemical species interconvert spontaneously because of equilibrium fluctuations during waiting time τ. (*b*) Nonequilibrium T2D-IR-EXSY. Interconversion is triggered by a VIS$_{pump}$ pulse during waiting time τ.

Here, we address the issue of the connectivity between the A and B substates, i.e., which A substate dissociates into which B substate, by monitoring their exchange cross-peaks with T2D-IR-EXSY. To this end, we selected a sw-Mb mutant where Val^{68} is replaced by Tyr (sw-Mb-V68Y). Its IR spectrum in the CO-bound form exhibits all of the essential A and B substates known from sw-MbCO. However, whereas A_3 is only a minority species in sw-MbCO, sw-MbCO-V68Y features comparable, large populations of the A_3 and A_1 conformational substates (10). In addition, we have performed the same experiment on horse heart Mb (h-MbCO). h-Mb differs in 18 amino acids from sw-Mb. It features mostly the A_1 conformation and almost no A_3, leading to simpler spectra suitable for illustrative purposes (18).

Experimental Strategy: 2D-IR-EXSY In and Out of Equilibrium

Equilibrium Experiment. In the pump probe implementation of 2D-IR-EXSY spectroscopy (pulse sequence in Fig. 1*a*) (3), a narrow-band femtosecond IR$_{pump}$ pulse is scanned over the frequency range of interest, defining the pump frequency axis of the 2D-IR spectrum (scheme in Fig. 2). After a waiting time τ, a broad-band IR$_{probe}$ pulse measures the response of the sample and is detected by a spectrometer, defining the probe frequency axis. The IR$_{pump}$ pulse transfers population from the $\nu = 0$ to the $\nu = 1$ state of the vibrational mode it is resonant with. The subsequent IR$_{probe}$ pulse encounters a depleted vibrational ground state, leading to a bleach contribution to the signal, and it encounters an excited-state population, leading to contributions caused by stimulated emission and excited-state absorption. As illustrated in Fig. 2*a*, this pulse sequence generates a diagonal peak for each mode, consisting of a negative contribution (blue, bleach, and stimulated emission) at its $\nu = 0 \rightarrow \nu = 1$ frequency ω_{01} and a positive contribution (red, excited-state absorption) at its $\nu = 1 \rightarrow \nu = 2$ frequency ω_{12}, which is lower

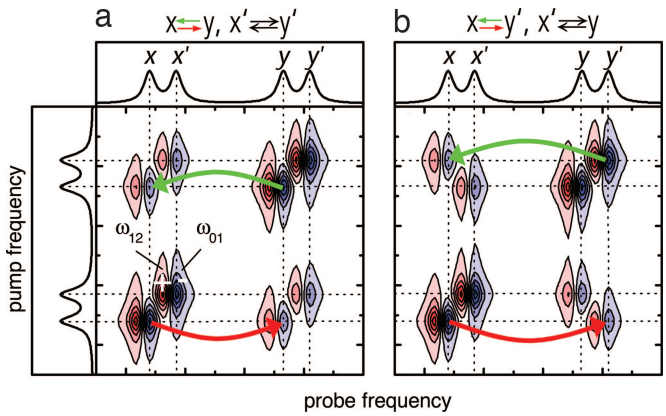

Fig. 2. Schematic 2D-IR-EXSY spectra illustrating the effect of different connectivities between the exchanging states *x*, *x*′, *y*, and *y*′. (*a*) Connectivity $x \leftrightarrows y$, $x' \leftrightarrows y'$. (*b*) Connectivity $x \leftrightarrows y'$, $x' \leftrightarrows y$.

because of vibrational anharmonicity. If two chemical species *x* and *y* interconvert in dynamic equilibrium ($x \rightleftarrows y$), and thereby change the frequency of a vibrational mode during the waiting time τ between IR$_{pump}$ and IR$_{probe}$, i.e., after it has been "labeled" by the IR$_{pump}$ pulse at a certain pump frequency, off-diagonal peaks are created, as indicated by the green and red arrows in Fig. 2. In this way, 2D-IR-EXSY maps the connectivity between interconverting chemical species (3, 5). We can, for example, distinguish the situation in Fig. 2*a*, where exchange occurs between *x* and *y* ($x \rightleftarrows y$) as well as between *x*′ and *y*′ ($x' \rightleftarrows y'$) from the situation in Fig. 2*b*, where we observe $x \rightleftarrows y'$ and $x' \rightleftarrows y$. The 2D-IR-EXSY approach is very general: in principle, all exchange processes that change an observable vibrational frequency can be investigated. A fundamental lower limit of its time window is caused by motional line narrowing, which leads to coalescence of the vibrational lines of the interconverting species if the exchange rates are on the order of the frequency separation between the vibrational bands or faster. A typical lower time limit is thus on the order of hundreds of femtoseconds; an upper time limit is imposed by vibrational relaxation. For example, the $\nu = 1$ state of CO in the B state of photolyzed carbonmonoxy hemoglobin relaxes with a 600-ps time constant (19). [The bound A state relaxes with a 17-ps (20, 21) time constant; however, this rate is not limiting our experiment as we photolyze the CO already after 1.5 ps.]

Nonequilibrium Experiment. Light-induced ligand migration is a nonequilibrium process, where exchange is triggered by an external perturbation, the VIS$_{pump}$ pulse, that dissociates the CO ligand from the heme. Therefore, instead of relying on equilibrium fluctuations during τ as in the 2D-IR-EXSY pulse sequence in Fig. 1*a*, we induce exchange by applying the VIS$_{pump}$ pulse during τ according to the pulse sequence in Fig. 1*b*. The method relies on the fact that vibrational excitation created in the initial state of the system by the IR$_{pump}$ pulse can be transferred to the photoproduct state. Additional vibrational excitation created by the trigger pulse does not interfere with the measurements because it is normalized out in the double difference 2D-IR spectra (22). By extending 2D-IR-EXSY to nonequilibrium T2D-IR-EXSY in this way, we can map the interconversion of species in a phototriggered process, and it is thus possible to obtain exchange cross-peaks between heme-bound CO and photodissociated CO in a docking site.

Results and Discussion

T2D-IR-EXSY of h-Mb^{13}CO: An Illustrative Example. Before turning to the experiment on sw-MbCO-V68Y, we first introduce T2D-IR-EXSY on h-MbCO because of its simpler CO stretching spectrum with essentially one single A_1 conformation around neutral pH (18). Fig. 3*a* shows the transient absorption spectrum of h-Mb^{13}CO in the region of the stretching absorption of the heme-bound CO ligand, 5 ps after 540-nm excitation at 294 K. Bleaching of the A_1 band occurs as the CO ligand is photodissociated from the heme iron. Concomitantly, the B bands emerge, shown in Fig. 3*b* for a delay of 5 ps. They indicate that the CO ligands have settled in the primary docking site B after photodissociation (13, 15, 23), where they reside for several nanoseconds before rebinding or escaping to secondary docking sites or exiting the protein. In addition to substates B_2 and B_1, corresponding to CO residing in the primary docking site in opposite orientations (15–17), weak hot bands of the CO ligand in the docking site are clearly visible in Fig. 3*b*, marked by ω_{12}. They are shifted by the CO anharmonicity of 26 cm^{-1}.

Fig. 3*c* shows the conventional 2D-IR spectrum of the heme-bound CO ligand, recorded with a delay $\tau = 1.5$ ps. The tilt of the band toward the diagonal indicates spectral inhomogeneity of the heme-bound CO, reflecting the heterogeneous structure of its protein surrounding (24).

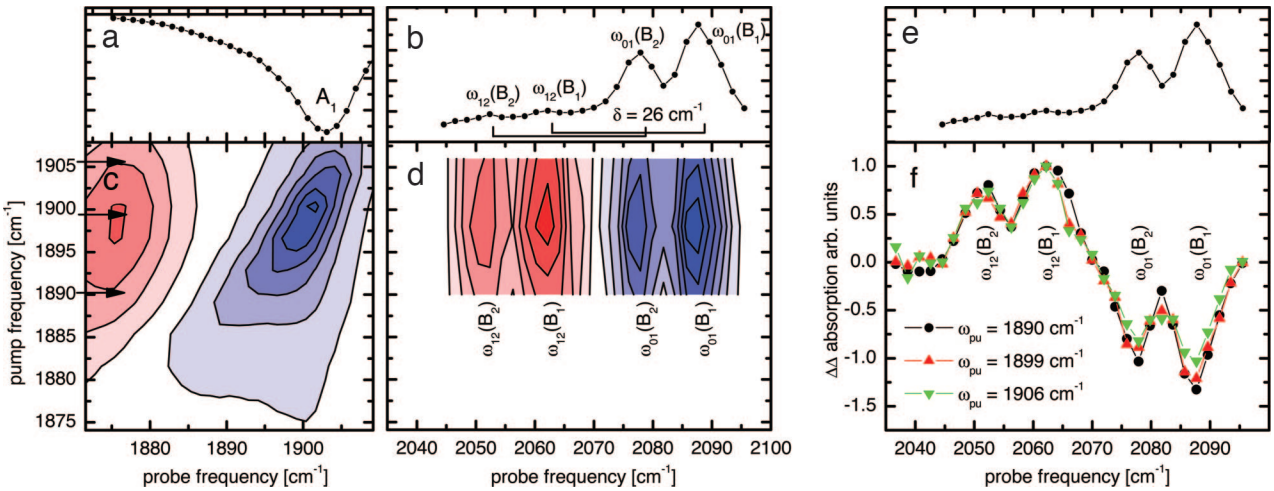

Fig. 3. 2D-IR spectroscopy of h-Mb^{13}CO. (*a*) Time-resolved IR spectrum of h-Mb^{13}CO, 5 ps after 540-nm excitation, showing the depletion of the heme-bound state. (*b*) Time-resolved IR spectrum of ^{13}CO migrated to the docking site, 5 ps after 540-nm excitation. B_2 and B_1 populations are generated. The rectangular brackets indicate the anharmonicity of CO of 26 cm^{-1}. Two small hot bands are visible here. (*c*) 2D-IR spectrum of the A state. Inhomogeneity leads to a tilt of the band toward the diagonal. (*d*) T2D-IR-EXSY spectrum of the cross-peaks connecting the A and B states. Delay IR_{pump}–VIS_{pump} was 1.5 ps; delay VIS_{pump}–IR_{probe} was 5.0 ps. (*e*) The same as *b* for comparison with *f*. (*f*) Normalized cuts through the exchange cross-peaks of *d*.

As the information on state connectivities in a 2D-EXSY spectrum is completely contained in the cross-peaks, we focused in our T2D-IR-EXSY measurements on the region of the exchange cross-peaks between heme-bound CO (A substates) and CO in the docking site (B substates). Fig. 3*d* shows the T2D-IR-EXSY cross peaks as recorded with the pulse sequence in Fig. 1*b*. The delay between IR_{pump} and VIS_{pump} was set to 1.5 ps. The delay between VIS_{pump} and IR_{probe} was set to 5.0 ps, as for the data in Fig. 3*b*. The narrow-band IR_{pump} labels the bound CO by transferring population from the $\nu = 0$ to the $\nu = 1$ state. Thus, in the cross-peak region, we expect to observe a bleach at the ω_{01} positions and an increased absorption from the vibrationally excited state at the ω_{12} positions (i.e., the positions of the hot bands in Fig. 3*b*) of the respective transitions. The signal in Fig. 3*d* clearly shows the success of the T2D-IR-EXSY experiment on ligand migration: exchange cross-peaks are observed between the heme-bound CO and the CO after ligand migration to the docking site. In contrast to the 2D-IR spectrum of the heme-bound CO ligand, spectral inhomogeneity cannot be observed for the cross-peaks.

In principle, the connectivity information in 2D-EXSY spectra is readily obtained from cuts through the cross-peak region at different IR_{pump} frequencies. For a more detailed view, Fig. 3*f* shows such cuts through the exchange cross-peaks in a normalized fashion. The ratios between B_1 and B_2 remain constant for the different IR_{pump} frequencies, indicating that B_2 and B_1 are populated in the same ratio, regardless of the initial starting frequency of the heme-bound CO ligand within the inhomogeneous A-band in Fig. 3*c*. Thus, the differences in the protein environment of the CO ligand leading to spectral inhomogeneity of the bound state either do not interfere with the pathways of the migrating ligands to the B site (which could imply that the structural heterogeneity at the binding site is quite local) or equilibration between the two CO orientations is already completed 5 ps after photodissociation, i.e., slightly earlier than reported (25).

Absorption Difference Spectra of sw-Mb^{13}CO-V68Y. After having demonstrated with h-Mb^{13}CO that T2D-IR-EXSY allows us to map ligand migration, we now turn to the case of sw-Mb^{13}CO-V68Y. Fig. 4*a* shows the FTIR absorption difference spectrum of sw-Mb^{12}CO-V68Y at 3 K in the C≡O stretching region of the ligand (adapted from ref. 10). Upon short (1 s) 532-nm illumination, bleaching of three bands is observed due to photodissociation of CO. These bands are essentially identical to the three conformational substates, A_3, A_1, and A_0 of WT-MbCO (10), indicating that the V68Y mutation causes only minor perturbations of the active site. However, in contrast to many

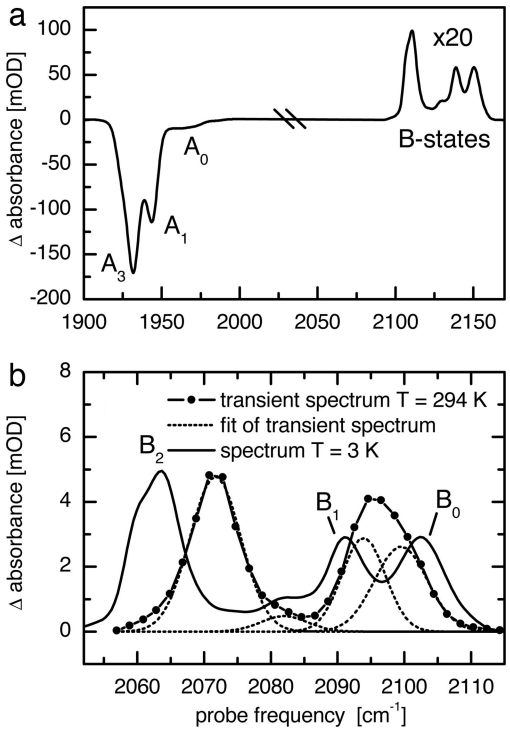

Fig. 4. IR spectra of sw-MbCO-V68Y. (*a*) FTIR absorption difference spectrum of sw-Mb^{12}CO-V68Y in cryosolvent (75% glycerol, 25% phosphate buffer, pH 8, illumination 1 s at 3 K, adapted from ref. 10). (*b*) Transient absorption difference spectrum of sw-Mb^{13}CO-V68Y 5 ps after 540-nm excitation at 294 K (scaled by ×5.5). The spectrum was fitted by four Gaussian lines. For comparison, the B-state spectrum from *a* is shown, shifted in frequency to account for ^{13}C labeling.

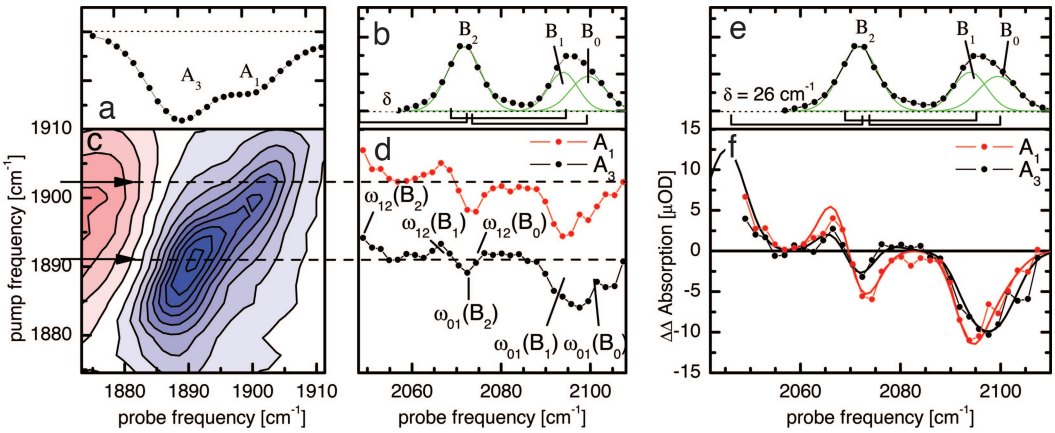

Fig. 5. 2D-IR spectroscopy of sw-MsCO-V68Y. (*a*) Time-resolved IR spectrum of sw-Mb^{13}CO-V68Y, 5 ps after 540-nm excitation. (*b*) Time-resolved IR spectrum of the ^{13}CO ligand in the primary docking site B, 5 ps after 540-nm excitation. B_2, B_1, and B_0 populations are observed. The square brackets at the bottom indicate the expected ω_{12} frequencies of the B_2, B_1, and B_0 substates. (*c*) 2D-IR spectrum of the A states. (*d*) Cuts through the T2D-IR-EXSY cross-peaks between heme-bound CO (A_1 and A_3) and CO in the docking site (B_2, B_1, and B_0). The IR_{pump} energies correspond to the respective arrows in *c*. (*e*) The same as *b* for orientation in *f*. (*f*) Overlay of the cross-peak cuts shown in *d*. The solid lines are calculated spectra.

other Mb variants, sw-Mb^{13}CO-V68Y features a large population in A_3, which is beneficial for the T2D-IR-EXSY experiments discussed here (10). The small population of A_0 at neutral pH will be neglected in the following discussion.

Concomitant with A band bleaching, the B bands emerge in the spectrum. The oscillator strength of CO reduces significantly upon dissociation from the heme; therefore, the B bands in Fig. 4*a* have been scaled up by a factor of 20. Fig. 4*b* shows the B-state spectrum under cryogenic conditions in an expanded view (black line). Several B substates are visible at frequencies similar to those of WT-MbCO, and they also show similar kinetic properties. Therefore, they have been termed B_2, B_1, and B_0 (10, 26). B_2 and B_1 are believed to correspond to CO residing in the primary docking site of Mb in the A_1 conformation in opposite orientations (10, 15–17). The larger stark splitting between B_2 and B_1 in sw-Mb^{13}CO-V68Y as compared with sw-Mb^{13}CO, which is also observed for the similar mutant V68F, has been attributed to the bulkier side chain of residue 68 that enhances the interaction between His^{64} and the CO ligand in the B state (10, 27). The substate B_0 has been associated with CO photodissociated from the A_3 conformation (10, 15, 28). However, as yet, a definitive structural assignment of the photoproduct associated with A_3 has been ambiguous. For CO in the primary docking site B, a similar splitting caused by reverse orientations as for B_2 and B_1 would be expected upon photodissociation from the A_3 conformation. Such a second band accompanying B_0 has not yet been observed. It was suggested to be either hidden underneath B_1 or not to be existent at all (28, 29), as the close proximity of His^{64} to the heme-bound CO in A_3 might enhance ligand translation to the B site without rotation after photodissociation (10). However, flipping of the CO orientation within the docking site was found to occur with a lifetime of ≈6 ps for h-Mb^{13}CO (25). Furthermore, earlier investigations of an orthorhombic crystal of Mb containing a dominant A_3 population (90%) at cryogenic temperatures indicated connectivities between A_3 and several B substates (28). Studies at ambient temperature have not been reported.

The transient spectrum recorded at 294 K, 5 ps after 540-nm excitation when the ligands settle in the docking site is shown as the blue line in Fig. 4*b*. It is different from the low-temperature steady-state spectrum (Fig. 4*b*, black line), and therefore, our assignment based on the comparison of band positions is only tentative. The B bands are shifted, causing a stronger overlap between B_1 and B_0 (see fit in Fig. 4*b*, dotted lines). The shoulder of B_2, clearly visible at 3 K, is not resolved in the transient measurement at 294 K. It is well known that the occupation ratios and exact positions of the CO bands in the low-temperature spectra depend on sample preparation, pH, and temperature, and the band positions can vary by a few wavenumbers. Moreover, with increasing temperature, bands shift and broaden because of increased librational motion (30, 31).

From the 1D spectra it is not clear which of the A substates is connected to which B substate. We will obtain this information from T2D-IR-EXSY.

T2D-IR-EXSY of sw-Mb^{13}CO-V68Y Reveals Connectivity of A and B Substates. Fig. 5*a* shows the time-resolved IR spectrum in the region of the heme-bound CO 5 ps after 540-nm excitation. The bleach of the A_1 and A_3 bands indicates CO release from the heme in both conformations. The CO ligand then enters the primary docking site B, as inferred from the appearance of the B substate bands in Fig. 5*b*. However, no conclusions can be drawn about the connectivities between A_3/A_1 and $B_2/B_1/B_0$ on the basis of the time-resolved 1D spectra.

Fig. 5*c* shows the conventional 2D-IR spectrum of heme-bound CO recorded with a delay of $\tau = 1.5$ ps. Both the A_3 and the A_1 conformations are clearly visible along the diagonal. Again, the blue (negative) part corresponds to the $\nu = 0 \rightarrow \nu = 1$ transition of the CO vibration, the red (positive) part corresponds to the $\nu = 1 \rightarrow \nu = 2$ transition.

Fig. 5*d* shows two cuts in the cross-peak region between A and B substates, obtained by the T2D-IR-EXSY pulse sequence depicted in Fig. 1*b*. The delay between IR_{pump} and VIS_{pump} was set to 1.5 ps, and the delay between VIS_{pump} and IR_{probe} was set to 5.0 ps, the same as in Fig. 5*b*. In the upper cut, the IR_{pump} pulse was set to 1,902 cm^{-1}, exciting predominantly CO ligands of the A_1 substate. In the lower cut, the IR_{pump} pulse was set to 1,891 cm^{-1}, exciting mainly CO ligands of the A_3 substate. However, because of the width of the IR_{pump} pulse of 11.5 cm^{-1} and the spectral overlap between the A_1 and the A_3 band, we achieve only partial selectivity of the IR excitation. For the upper and lower cuts, the excitation ratios are A_1/A_3 = 7:3 and A_1/A_3 = 3:7, respectively.

Because of the presence of several overlapping bands, the cross-peak signal in Fig. 5*d* is more complicated than for h-Mb^{13}CO. The IR_{pump} pulse tags the CO ligands of the two conformational substates A_3 and A_1 by vibrational excitation before they start their migration to the B substates. Thus, as for

h-Mb^{13}CO, we find a depletion in the cross-peak cuts at the frequencies ω_{01} involving the vibrational ground states. This can be clearly seen in the region of 2,085–2,110 cm^{-1}, containing ω_{01} (B_1) and ω_{01} (B_0). For the B_2 band, however, its negative ω_{01} (B_2) contribution overlaps with the positive ω_{12} contributions from B_1 and/or B_0. The ω_{12} (B_2) cross-peak lies at the low-frequency edge of the spectral window observed here.

The cross-peak cuts for A_3 and A_1 in Fig. 5*d* look very similar. In particular, the similar shapes of the two cuts at the B_2 frequency clearly reveal a negative contribution at ω_{01} (B_2) for ligands photodissociated from A_1 and A_3, indicating population transfers $A_1 \rightarrow B_2$ and $A_3 \rightarrow B_2$. If CO photodissociated from A_3 gave rise to B_0 and A_1 to B_2 and B_1, only a positive contribution at ω_{12} (B_0) would be observed in the A_3 cut.

A direct comparison of the cross-peak cuts for A_3 and A_1 is given in Fig. 5*f*, with the transient absorption spectrum of the B substates plotted above (Fig. 5*e*) for orientation. In the region of ω_{01} (B_1) and ω_{01} (B_0), the cut through A_1 is clearly red-shifted compared with the A_3 cut, indicating increased population transfer to B_1. The cut through A_3 is shifted to the blue, indicating increased population transfer to B_0. In the ω_{01} (B_2) region, the amplitude of the A_3 cut is smaller then the one of the A_1 cut. This also is a consequence of the population of B_0 when starting from A_3: its ω_{12} (B_0) contribution is closer to the ω_{01} band of B_2 than the ω_{12} contribution of B_1, causing stronger cancellation.

To rationalize the effect of the incomplete selectivity of the IR_{pump} pulse regarding A_1 and A_3, we calculated the T2D-IR-EXSY cross-peaks (solid lines in Fig. 5*f*) based on the fit of the absorption spectrum, i.e., the green lines in Fig. 5*e*. The calculation takes into account the finite width of the IR_{pump} pulse and the band shape of the A_1 and A_3 bands. The connectivities $A_3 \rightarrow (B_0,B_2)$ and $A_1 \rightarrow (B_1,B_2)$ are assumed as well as equal population of the two respective B states in each case. The agreement with the data, also in the region of the B_2 state, confirms the assignment $A_3 \rightarrow (B_0,B_2)$ and $A_1 \rightarrow (B_1,B_2)$.

A possible explanation for the population transfer from both A_3 and A_1 to B_2 is that the B_2 band in fact consists of two bands, one connected to A_1 as suggested before and one connected to A_3, which we will call $B_2(A_3)$. We thus have the connectivities $A_3 \rightarrow (B_0,B_2(A_3))$ and $A_1 \rightarrow (B_1(A_1),B_2(A_1))$, where B_2 and B_1 are counterparts with opposite orientation of CO. Because of the analogy between A_1 and A_3 it appears likely that the $B_2(A_3)$ band is the elusive counterpart of B_0 with CO in the reverse orientation. We therefore suggest to rename the B states connected to A_3 in analogy to the states connected to A_1: B_0 as $B_1(A_3)$ and $B_2(A_3)$, assigned to opposite orientations of CO. The finding that B_2 is composed of two subbands fits well to the observation of the substructure of B_2 in the low-temperature difference spectrum in Fig. 4*b*.

Further support for the assignment found by T2D-IR-EXSY for physiological temperature was obtained from FTIR temperature derivative spectroscopy (TDS; ref. 10) at cryogenic temperatures. One-second irradiation with 532-nm light at 3 K prepared a sw-MbCO-V68Y sample in a photodissociated nonequilibrium state. It subsequently was heated at a rate of 5 mK/s in the dark while FTIR spectra were taken continuously, one every kelvin, to monitor equilibration between the B states. Note that these experiments have been carried out with ^{12}CO. Fig. 6*b* shows differences between consecutive spectra as a 2D-TDS contour map, spanned by the temperature and wavenumber axes. Absorbance decreases at 2,111 and 2,107 cm^{-1} (dotted contours) with concomitant increases at 2,139 and 2,150 cm^{-1} (solid contours) represent reorientation of the CO ligands in docking site B for substates A_1 and A_3, respectively. To separate the B_2 signals of A_1 and A_3, we performed a second experiment, in which the sample was heated to 50 K under 532-nm illumination and afterward cooled to 3 K in the dark. With this preparation,

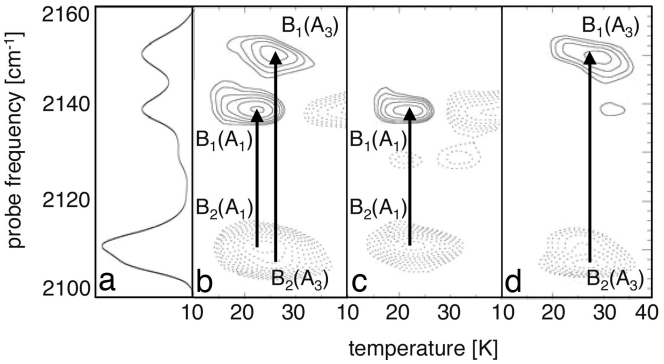

Fig. 6. FTIR-TDS spectroscopy of sw-Mb^{12}CO-V68Y. (*a*) Absorption spectrum of the B states as in Fig. 3*b*. (*b–d*) FTIR-TDS maps of sw-Mb^{12}CO-V68Y, showing absorption changes that are associated with ^{12}CO reorientation in the B site for A_1 and A_3 (*b*) and the separated reorientation signals for A_1 (*c*) and A_3 (*d*).

the A_1 population rebounded again, whereas A_3 remained photolyzed because of its higher rebinding barriers (8, 10). After another 1-s illumination at 3 K, FTIR spectra were taken with increasing temperature as in the previous experiment. The contour plot in Fig. 6*c* shows ligand reorientation only for the B states belonging to A_1 because reorientation of CO for substate A_3 already occurred during the first temperature excursion. The difference plot between the data in Fig. 6 *b* and *c*, plotted in Fig. 4*d*, shows the reorientation signal for A_3. Clearly, the B_2 band consists of two subbands of slightly different frequency, one connected to $B_1(A_1)$ and one to $B_1(A_3)$.

The FTIR-TDS results strongly support our assignment of the T2D-IR-EXSY spectra at physiological temperature, where we found the connectivities $A_1 \rightarrow (B_1(A_1),B_2(A_1))$ and $A_3 \rightarrow (B_1(A_3),B_2(A_3))$. This assignment corresponds to a Stark splitting between $B_1(A_3)$ and $B_2(A_3)$ that is slightly increased as compared with the one between $B_1(A_1)$ and $B_2(A_1)$. However, this finding is not unexpected as the interaction between His^{64} and the CO in the docking site should be larger for A_3 than for A_1, leading to stronger electrostatic interactions (10).

Conclusions

T2D-IR-EXSY is a vibrational analog of 2D-NMR-EXSY working under nonequilibrium conditions. It maps the connectivity of interconverting species during light-induced nonequilibrium processes with subpicosecond time resolution. In the present work, T2D-IR-EXSY allowed us to track the light-induced migration of CO ligands in Mb from the binding site A to the primary docking site B on the escape pathway of the ligand.

Exchange cross-peaks revealed the connectivity between the conformational substates A_3/A_1 of the protein:ligand complex with CO at the binding site and the substates $B_2/B_1/B_0$ of the protein:ligand complex with CO in the primary docking site. We have shown that the B_2 band in fact consists of two bands, one of them being the elusive counterpart of B_0 with opposite CO orientation. This interpretation is strongly supported by FTIR-TDS. In summary, we suggest an assignment where each of the conformational substates A_3 and A_1 supports two docking site states B_2 and B_1 with opposite CO orientation: $A_3 \rightarrow (B_2(A_3),B_1(A_3))$ and $A_1 \rightarrow (B_2(A_1),B_1(A_1))$.

FTIR-TDS has been used here as an independent method to support the T2D-IR-EXSY assignment. It is similar to T2D-IR-EXSY in that it also obtains connectivity information by monitoring relaxation in a nonequilibrium ensemble, however, at cryogenic temperatures. While T2D-IR-EXSY uses high time resolution to investigate short-lived intermediates that can be selectively addressed by the IR_{pump} pulse, FTIR-TDS relies on trapping intermediates at low temperatures and selects them via

the activation energy of their relaxation. The compatibility of cryo FTIR-TDS results and the findings of T2D-IR-EXSY at physiological temperatures indicates that the assumption usually made in cryo trapping experiments, namely that the trapped state exist similarly also at physiological temperatures, is well justified for the system investigated here.

T2D-IR-EXSY provides a solution to the longstanding problem of correlating rapidly interconverting substates at physiological temperatures. Here, we have demonstrated the use of T2D-IR-EXSY to map the migration of ligands between different sites in a protein. The T2D-IR-EXSY approach, however, is very general; the prerequisite is just the change of a vibrational frequency on the course of the investigated process within the time window of the experiment. Therefore it should be well applicable to other light-induced processes in chemistry, physics, and biology, such as photochemical reactions, electron transfer, proton transfer, or phototriggered conformational changes.

Materials and Methods

Sample Preparation. Plasmids containing the sw-Mb-V68Y mutant gene were transformed into *Escherichia coli*, strain TB1, expressed, and purified as described (32). h-Mb was purchased from Sigma/Aldrich (St. Louis, MO) and used without further purification. Samples for spectroscopy were prepared by dissolving the lyophilized protein at a concentration of 15 mM in deuterated phosphate buffer (pD 8, 100 mM) and subsequent reduction with excess dithionite under a ^{13}CO atmosphere. For time-resolved experiments, the sample solution was circulated in a closed-cycle CaF_2 flow cell (path length 50 μm, cycle volume 450 μl) (33).

Spectroscopy Setup. T2D-IR spectra were recorded as described (34). The output of a 1-kHz titanium-doped sapphire oscillator/regenerative amplifier femtosecond laser system was frequency converted to obtain VIS_{pump} pulses for optical triggering of the ligand migration and mid-IR pulses for time-resolved 1D and 2D-IR spectroscopy. VIS_{pump} pulses (500 fs, 540 nm, 2.0 μJ) were generated in a single-stage noncollinear optical parametric amplifier used without compression and focused into the flow cell to a spot size of 120 μm. Mid-IR pulses (100 fs, 1,910 cm^{-1}, bandwidth 240 cm^{-1} FWHM, 2.6 μJ) were generated in a white light-seeded, two-stage β-barium borate optical parametric amplifier with a subsequent $AgGa_2S_4$-based difference frequency mixing stage (35). A small fraction of the IR pulses was split off to obtain broadband IR_{probe} and $IR_{reference}$ pulses. The remainder was passed through a computer-controlled Fabry-Perot interferometer to generate narrow-band (11.5 cm^{-1}), tunable IR_{pump} pulses. IR_{pump} and IR_{probe} were focused into the sample to a spot size of 120 and 80 μm, respectively, in spatial overlap with the VIS_{pump} from the noncollinear optical parametric amplifier. The $IR_{reference}$ passed the flow cell 1 mm upstream. IR_{probe} and $IR_{reference}$ were dispersed in a spectrograph and imaged onto a 2×32-pixel HgCdTe detector array that enabled us to measure low noise (typically 0.04 mOD rms for 100 shots averaging) transient spectra with a spectral resolution of 2 cm^{-1}.

1. Meier BH, Ernst RR (1979) *J Am Chem Soc* 101:6441–6442.
2. Kubo R (1969) *AIP Conf Proc* 14:101–127.
3. Woutersen S, Mu Y, Stock G, Hamm P (2001) *Chem Phys* 266:137–147.
4. Kim YS, Hochstrasser RM (2005) *Proc Natl Acad Sci USA* 102:11185–11190.
5. Zheng J, Kwak K, Asbury J, Chen X, Oiletic IR, Fayer MD (2005) *Science* 309:1338–1343.
6. Bredenbeck J, Helbing J, Hamm P (2004) *J Am Chem Soc* 126:990–991.
7. Frauenfelder H, McMahon BH, Fenimore PW (2003) *Proc Natl Acad Sci USA* 100:8615–8617.
8. Johnson JB, Lamb DC, Frauenfelder H, Müller JD, McMahon B, Nienhaus GU, Young RD (1996) *Biophys J* 71:1563–1573.
9. Vojtìchovský J, Chu K, Berendzen J, Sweet RM, Schlichting I (1999) *Biophys J* 77:2153–2174.
10. Nienhaus K, Deng P, Olson JS, Warren JJ, Nienhaus GU (2003) *J Biol Chem* 278:42532–42544.
11. Yang F, Phillips, GN, Jr (1996) *J Mol Biol* 256:762–774.
12. Müller JD, McMahon BH, Chien EYT, Sligar SG, Nienhaus GU (1999) *Biophys J* 77:1036–1051.
13. Lim M, Jackson TA, Anfinrud PA (1995) *J Chem Phys* 102:4355–4366.
14. Lim M, Jackson TA, Anfinrud PA (1995) *Science* 269:962–966.
15. Nienhaus K, Olson JS, Franzen S, Nienhaus GU (2005) *J Am Chem Soc* 127:40–41.
16. Lim M, Jackson TA, Anfinrud PA (1997) *Nat Struct Biol* 4:209–214.
17. Nutt DR, Meuwly M (2003) *Biophys J* 85:3612–3622.
18. Nienhaus GU, Mourant JR, Chu K, Frauenfelder H (1994) *Biochemistry* 33:13413–13430.
19. Sagnella DE, Straub JE, Jackson TA, Lim M, Anfinrud PA (1999) *Proc Natl Acad Sci USA* 96:14324–14329.
20. Hill JR, Tokmakoff A, Peterson KA, Sauter B, Zimdars D, Dlott DD, Fayer MD (1994) *J Phys Chem* 98:11213–11219.
21. Owrutsky JC, Li M, Locke B, Hochstrasser RM (1995) *J Phys Chem* 99:4842–4846.
22. Bredenbeck J, Helbing J, Hamm P (2004) *J Chem Phys* 121:5943–5957.
23. Schotte F, Lim M, Jackson TA, Smirnov AV, Soman J, Olson JS, Phillips GN, Jr, Wulff M, Anfinrud PA (2003) *Science* 300:1944–1947.
24. Merchant KA, Noid WG, Akiyama R, Finkelstein IJ, Goun A, McClain BL, Loring RF, Fayer MD (2003) *J Am Chem Soc* 125:13804–13818.
25. Kim S, Lim M (2005) *J Am Chem Soc* 127:5786–5787.
26. Alben JO, Beece D, Bowne SF, Doster W, Eisenstein L, Frauenfelder H, Good D, McDonald JD, Marden MC, Moh PP, *et al.* (1982) *Proc Natl Acad Sci USA* 79:3744–3748.
27. Olson JS, Phillips GN, Jr (1996) *J Biol Chem* 271:17593–17596.
28. Mourant JR, Braunstein DP, Chu K, Frauenfelder H, Nienhaus GU, Ormos P, Young RD (1993) *Biophys J* 65:1496–1507.
29. Nienhaus K, Deng P, Kriegl JM, Nienhaus GU (2003) *Biochemistry* 42:9647–9658.
30. Kriegl JM, Nienhaus K, Deng P, Fuchs J, Nienhaus GU (2003) *Proc Natl Acad Sci USA* 100:7069–7074.
31. Helbing J, Nienhaus K, Nienhaus GU, Hamm P (2005) *J Chem Phys* 122:124505.
32. Springer BA, Sligar SG (1987) *Proc Natl Acad Sci USA* 84:8961–8965.
33. Bredenbeck J, Hamm P (2003) *Rev Sci Instrum* 74:3188–3189.
34. Bredenbeck J, Helbing J, Behrendt R, Renner C, Moroder L, Hamm P (2003) *J Phys Chem B* 107:8654–8660.
35. Hamm P, Kaindl RA, Stenger J (2000) *Opt Lett* 25:1798–1800.